Eastern Pacific ITCZ Dipole and ENSO Diversity

SHANG-PING XIE,[a,b,c] QIHUA PENG,[d,e,a] YOUICHI KAMAE,[f,a], XIAO-TONG ZHENG,[b,c] HIROKI TOKINAGA,[g] AND DONGXIAO WANG[d]

[a] *Scripps Institution of Oceanography, University of California, San Diego, La Jolla, California*
[b] *Physical Oceanography Laboratory, Ocean University of China, Qingdao, China*
[c] *Qingdao National Laboratory for Marine Science and Technology, Qingdao, China*
[d] *State Key Laboratory of Tropical Oceanography, South China Sea Institute of Oceanology, Chinese Academy of Sciences, Guangzhou, China*
[e] *University of Chinese Academy of Sciences, Beijing, China*
[f] *Faculty of Life and Environmental Sciences, University of Tsukuba, Tsukuba, Japan*
[g] *Hakubi Center for Advanced Research and Disaster Prevention Research Institute, Kyoto University, Uji, Japan*

(Manuscript received 29 December 2017, in final form 22 February 2018)

ABSTRACT

The eastern tropical Pacific features strong climatic asymmetry across the equator, with the intertropical convergence zone (ITCZ) displaced north of the equator most of time. In February–April (FMA), the seasonal warming in the Southern Hemisphere and cooling in the Northern Hemisphere weaken the climatic asymmetry, and a double ITCZ appears with a zonal rainband on either side of the equator. Results from an analysis of precipitation variability reveal that the relative strength between the northern and southern ITCZ varies from one year to another and this meridional seesaw results from ocean–atmosphere coupling. Surprisingly this meridional seesaw is triggered by an El Niño–Southern Oscillation (ENSO) of moderate amplitudes. Although ENSO is originally symmetric about the equator, the asymmetry in the mean climate in the preceding season introduces asymmetric perturbations, which are then preferentially amplified by coupled ocean–atmosphere feedback in FMA when deep convection is sensitive to small changes in cross-equatorial gradient of sea surface temperature. This study shows that moderate ENSO follows a distinct decay trajectory in FMA and southeasterly cross-equatorial wind anomalies cause moderate El Niño to dissipate rapidly as southeasterly cross-equatorial wind anomalies intensify ocean upwelling south of the equator. In contrast, extreme El Niño remains strong through FMA as enhanced deep convection causes westerly wind anomalies to intrude and suppress ocean upwelling in the eastern equatorial Pacific.

1. Introduction

El Niño–Southern Oscillation (ENSO) is the dominant mode of interannual variability, which arises from the zonal interaction of the tropical Pacific Ocean and atmosphere. While Bjerknes (1969) originally envisioned that the weakened easterly winds reduce local ocean upwelling and cause the equatorial Pacific to warm, Wyrtki (1975) noted that the local trade winds hardly change over the eastern Pacific during El Niño and sea surface temperature (SST) increase is caused by the anomalously deepened thermocline. In fact, wind variations are typically confined to the western half of the equatorial Pacific while SST anomalies extend and often amplify toward the South American coast (Deser and Wallace 1990). Now it is widely accepted that the westerly wind anomalies in the central Pacific depress the thermocline through equatorial wave adjustments and cause the eastern Pacific to warm. Composite analysis that isolates common features of ENSO events was instrumental in developing this classic view of the ENSO phenomenon.

Each El Niño is different. With more observations, there are increasing interests in studying differences among ENSO events. Some classify ENSO events based on the SST pattern (Ashok et al. 2007; Kug et al. 2009; Kao and Yu 2009; Takahashi et al. 2011), that is, whether SST anomalies are larger in the eastern (Niño-3 region: 5°S–5°N, 150°–90°W) or central (Niño-4 region: 5°S–5°N, 160°E–150°W) equatorial Pacific. Others emphasize the difference in rainfall anomalies averaged in the Niño-3 region of the eastern equatorial Pacific (Chiodi and Harrison 2013; Cai et al. 2014), noting the importance for atmospheric teleconnections (Johnson and Kosaka 2016;

Corresponding author: Shang-Ping Xie, sxie@ucsd.edu

DOI: 10.1175/JCLI-D-17-0905.1

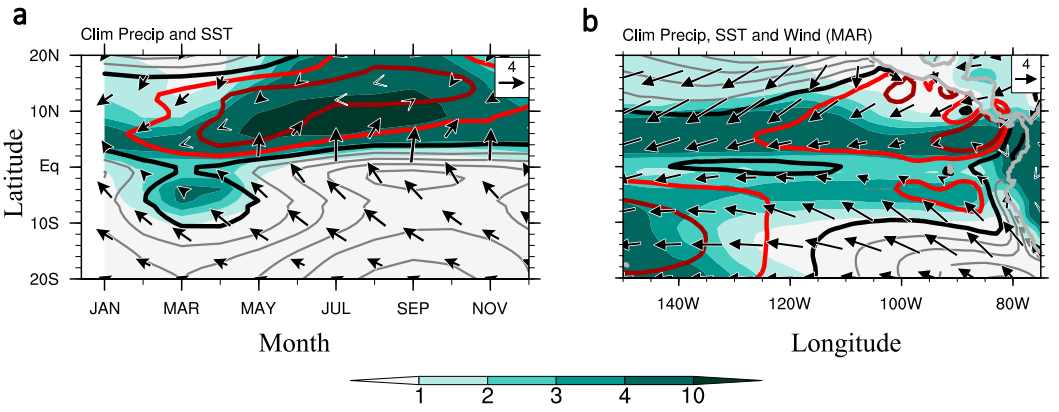

FIG. 1. Climatology of SST (contours at intervals of 1°C; the 26.5°C contour highlighted in thick black, 27.5°C in red, and 28.5°C in dark red), precipitation (mm day^{-1}; shading) and surface wind velocity (m s^{-1}; vectors): (a) time–latitude section zonally averaged in 140°–80°W, and (b) in March.

Siler et al. 2017). SST and rainfall averaged in the Niño-3 region are designed to capture equatorially peaked phenomena, a pattern that SST anomalies of ENSO indeed fit. It is unclear whether the Niño-3 means are always appropriate to capture major modes of eastern tropical Pacific variability. For example, ENSO-induced changes in deep convection tend to be confined north of the equator most of time, a meridional structure not well captured by averages in the equatorially centered Niño-3 region. This asymmetry in atmospheric anomalies of ENSO is due to the meridional asymmetry of the eastern Pacific climate, where SSTs on and south of the equator are generally below the convective threshold (~26.5°–27°C in current climate; Johnson and Xie 2010), and the intertropical convergence zone (ITCZ) is displaced north of the equator (Xie 2004).

In March, SST reaches the annual minimum in the Northern Hemisphere and the annual maximum in the Southern Hemisphere. This seasonal pattern opposes and nearly balances the annual-mean asymmetry, and at the spring equinox, the eastern tropical Pacific climate is nearly symmetric about the equator (Fig. 1b). A double ITCZ appears briefly during boreal spring [February–April (FMA)] (Fig. 1a), with a zonal rainband on either side of the equator across the eastern half of the tropical Pacific Ocean (Kornfield et al. 1967). As the southerly cross-equatorial winds slow, upwelling weakens and SST rises near the equator (Mitchell and Wallace 1992; Xie 1994), although SSTs at the equator remain slightly below the convective threshold. As a result, FMA is a time when atmospheric deep convection is sensitive to small changes in SST near the equator. While ENSO at the peak phase of November–January (NDJ) has been studied extensively, variability in FMA has not received as much attention when ENSO starts to decay and the local coupling between SST and deep convection strengthens over the eastern tropical Pacific.

This motivates our study that focuses on FMA variability in the eastern Pacific ITCZ over the satellite era. Our results reveal a previously unknown mode of ocean–atmosphere interaction unique to FMA, which is characterized by a basin-scale meridional dipole of rainfall anomalies across the equator and manifested as interannual variability in the relative intensity between the northern and southern ITCZs. Surprisingly, this meridional mode is closely related to the decay of ENSO events. Recent studies show considerable variability in SST decay among El Niño events (Lengaigne and Vecchi 2010) and between El Niño and La Niña (Okumura and Deser 2010). Such diversity in ENSO decay has important effects on the Indo-western Pacific summer climate (Ohba and Ueda 2006; Xie et al. 2010; Yang et al. 2015; Ma et al. 2017a).

The next section introduces data used in this study. Sections 3 and 4 present leading modes of convective variability over the eastern tropical Pacific and discuss the coupled dynamics. Section 5 shows that these modes are robust in ship observations over a longer period after 1950. Section 6 summarizes the results in the context of the literature in ENSO diversity.

2. Data

We use the following datasets: the Climate Prediction Center (CPC) Merged Analysis of Precipitation (CMAP; https://www.esrl.noaa.gov/psd/data/gridded/data.cmap.html), derived from satellite observations and available since 1979 on a 2.5° × 2.5° grid (Xie and Arkin 1997); the NOAA Optimum Interpolation Sea Surface Temperature, version 2 data (OISST; https://www.esrl.noaa.gov/psd/data/gridded/data.noaa.oisst.v2.html), available since 1982 on a 1° × 1° grid (Reynolds et al. 2002); surface heat flux from the Air–Sea Fluxes for

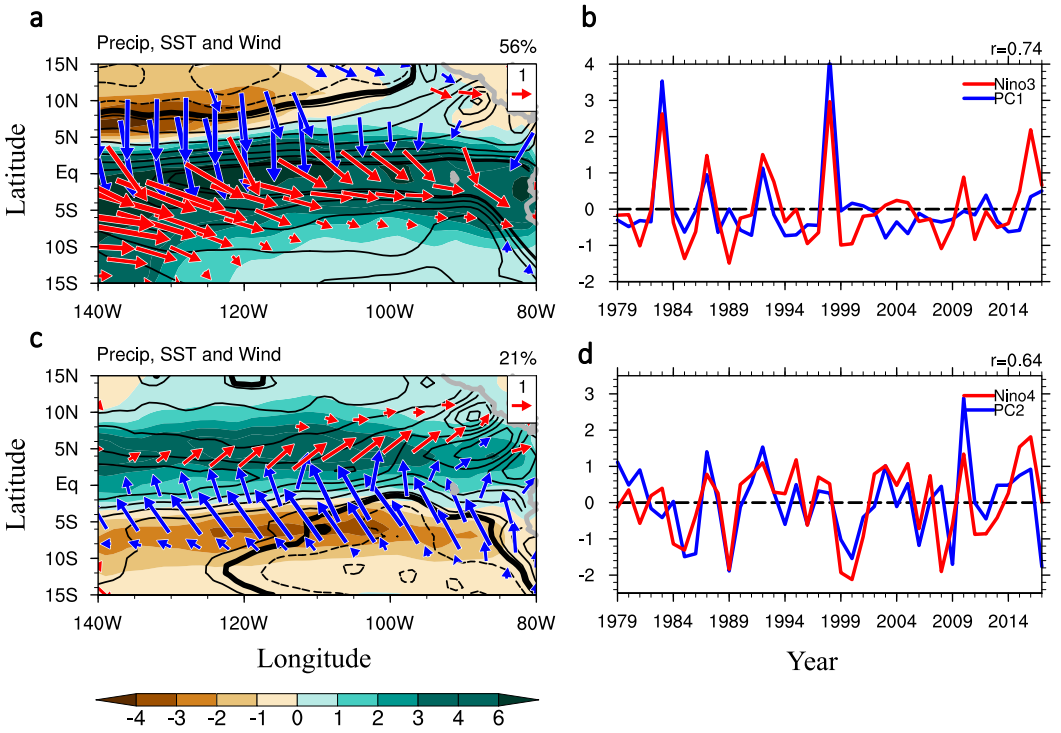

FIG. 2. EOF modes of FMA rainfall variability over the eastern tropical Pacific. (a),(c) Regressions of rainfall (color shading), SST (contours at intervals of 0.3°C, zero thickened and negative dashed), and surface wind ($m\,s^{-1}$; vectors) against (b),(d) the standardized PCs (blue). Also plotted in red are concurrent (b) eastern (Niño-3) and (d) central (Niño-4) equatorial Pacific SST indices (standardized). Blue (red) arrows in (a),(c) indicate wind anomalies that strengthen (weaken) climatological winds. The correlations (r) are significant at the 95% confidence level based on a t test.

the Global Tropical Oceans (TropFlux) project (http://www.incois.gov.in/tropflux/) for 30°S–30°N on a 1° × 1° grid (Kumar et al. 2012); wind velocity and specific humidity from the ECMWF interim reanalysis (ERA-Interim; http://apps.ecmwf.int/datasets/data/interim-full-daily/levtype=sfc/) for 1979 to 2017 on a 1° × 1° grid (Dee et al. 2011); and ocean temperature from the NCEP Global Ocean Data Assimilation System (GODAS; https://www.esrl.noaa.gov/psd/data/gridded/data.godas.html) on a 1° × (1/3)° grid. The Extended Reconstructed SST (ERSST) dataset (Huang et al. 2015) is used to compute regional SST indices for the equatorial Pacific, including the Niño-3.4 (5°S–5°N, 170°–120°W) and Niño-1+2 (0°–10°S, 90°–80°W) regions.

Prior to the satellite era, we use precipitation from the European Twentieth Century Reanalysis (ERA-20C) for 1950–2010 on a 1° × 1° grid (Poli et al. 2016); and surface wind velocity, marine cloudiness, and SST in the International Comprehensive Ocean–Atmosphere Data Set (ICOADS) for 1950–2017 (Freeman et al. 2017). For stable statistics, ICOADS ship reports are gridded on a coarse 4° × 4° grid without interpolation. Over warm tropical oceans, ship-observed cloudiness is often a good proxy of deep convective activity. ERA-20C assimilates ICOADS sea level pressure and surface winds, along with observed SST and sea ice as surface boundary conditions.

We use an atmospheric simulation forced by the observed evolution of SST, sea ice, and radiative forcing for 1951–2010, from the database for Policy Decision Making for Future Climate Change (d4PDF; Mizuta et al. 2017). The atmospheric general circulation model, developed at the Japan Meteorological Research Institute, is spectral with effective resolution of 60 km and 64 vertical levels. An ensemble of 100 runs was conducted with slightly different initial conditions and to sample uncertainties in prescribed boundary conditions. The ensemble mean is analyzed to evaluate atmospheric response to SST, sea ice, and radiative forcing.

3. Extreme El Niño

We perform an empirical orthogonal function (EOF) analysis on CMAP precipitation averaged for FMA during the 39-yr period of 1979–2017 in the eastern tropical Pacific domain of 15°S–15°N, 140°–80°W. The 1979–2017 mean is taken as the climatology. As will become clear, convective variability in this region is

important for ENSO evolution by affecting surface winds and hence ocean upwelling.

The leading EOF mode of FMA rainfall variability, accounting for 56% of total variance, features increased rainfall centered on the equator (Fig. 2a). It captures so-called extreme El Niño events with strong convection (Chiodi and Harrison 2013; Johnson and Kosaka 2016) and heavy rainfall in the Niño-3 region of the eastern Pacific (Cai et al. 2014; Takahashi et al. 2011). The principal component (PC) is dominated by the 1983 and 1998 major El Niño events and includes two weaker events of 1987 and 1992. Even in the warm season of FMA, climatological mean SSTs over the eastern equatorial Pacific are still below the threshold for deep convection (~27°C, Fig. 1) so only El Niño events of considerable warming in the Niño-3 region can cause deep convection (Zheng et al. 2016). This SST threshold explains why PC1 is strongly skewed positively—there is no extreme La Niña. PC1 is correlated with Niño-3 SST ($r = 0.74$) but the variability is muted in the negative regime compared to SST. The correlation with SST is due to the four extreme El Niño events and is not expected for weak SST variability without much of an effect on deep convection. Interestingly, PC1 varies little after 1998 (Lee and McPhaden 2010). It is interesting to note that PC1 is only weakly positive in 2016 following a major El Niño.

Because of the subcritical mean SST for deep convection on the equator, most El Niño of moderate amplitude and all La Niña do not cause changes in overall Niño-3 convective activity over the eastern Pacific and hence in zonal atmospheric pressure gradient. As a result, zonal wind hardly varies over the eastern equatorial Pacific (Deser and Wallace 1990), inspiring the classic idea that El Niño is caused by the deepened thermocline in response to remote wind forcing (Wyrtki 1975). By raising SST above the convective threshold, extreme El Niño intensifies deep convection over the eastern equatorial Pacific. The convective heating causes westerly wind anomalies to intrude into the eastern equatorial Pacific (Fig. 2a), and the reduced equatorial upwelling sustains the eastern Pacific warming through FMA (Lengaigne and Vecchi 2010). The intrusion of the westerly anomalies and the eastern Pacific warming form a positive feedback, counteracting the rapid decay of the equatorial wind anomalies in the central Pacific after December (e.g., Vecchi and Harrison 2006; McGregor et al. 2012).

The termination of the 1998 El Niño is a good example (Fig. 3). By April, the thermocline depth at 0°, 125°W has returned to normal but pronounced westerly wind anomalies remain in response to intense convection that occupies the eastern equatorial Pacific all the way to the

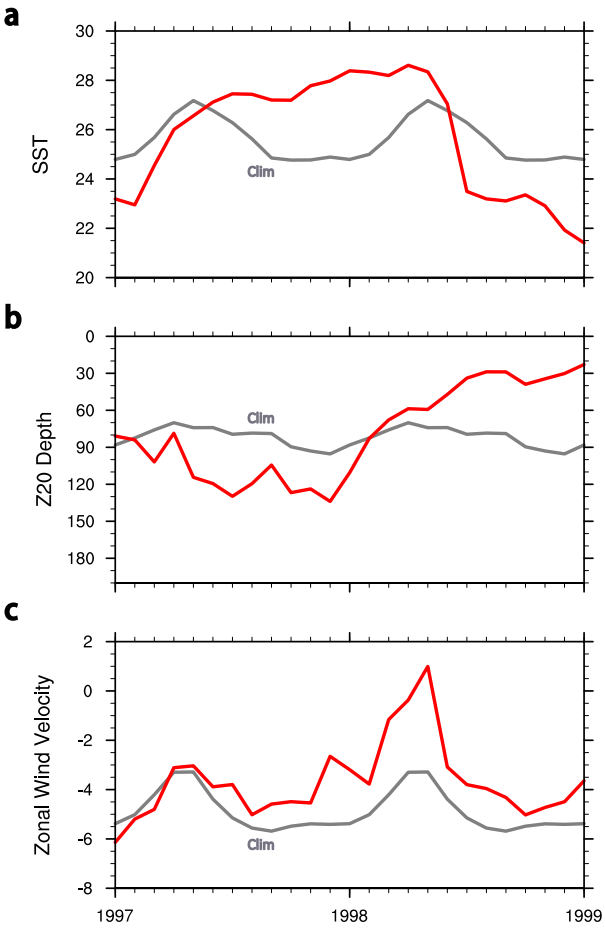

FIG. 3. Evolution of the 1997/98 El Niño. (a) SST (°C), (b) the depth of the 20°C isotherm (m), and (c) zonal wind velocity ($m\,s^{-1}$). Analyses are based on monthly averages between 2°N and 2°S for the TAO data. The climatology is plotted in gray as reference.

South American coast. The westerly wind anomalies keep equatorial upwelling in check until May when a strong Madden–Julian oscillation brings easterly winds back to the eastern equatorial Pacific (Takayabu et al. 1999). The resumed upwelling causes SST at this site to drop by 5°C within the month of May 1998 (McPhaden 1999). This illustrates that the shoaling thermocline is a necessary but not sufficient condition, and the local westerly wind anomalies delay and control the timing of the surface cooling following an extreme Niño.

4. Meridional seesaw

EOF2, accounting for 21% of the variance, features a meridional dipole that is nearly zonally uniform east of 140°W (Fig. 2c). The band of increased (decreased) rainfall is centered at 5°N (6°S), roughly collocated with the FMA climatological rainband. The meridional dipole is associated with a deep anomalous cross-equatorial

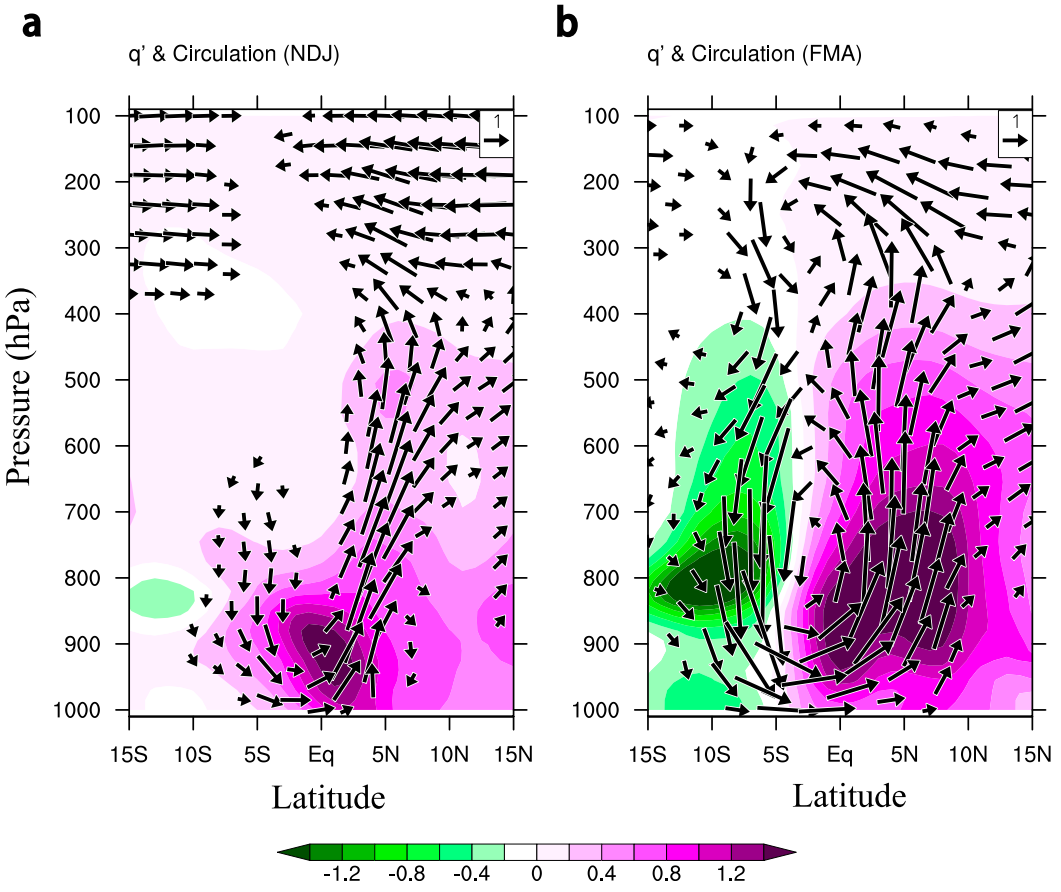

FIG. 4. Vertical circulation anomalies of the EPID mode. Regressions against the FMA rainfall PC2 of (a) NDJ and (b) FMA vertical circulation (m s^{-1}; arrows) and specific humidity (q', g kg^{-1}; color shading), zonally averaged in 140°–80°W.

Hadley cell that extends over the entire troposphere (Fig. 4b). This, along with the deep anomalies of specific humidity, indicates that the rainfall dipole results from a reorganization of deep convection over the eastern equatorial Pacific. Thus, EOF2 represents interannual variability in the relative intensity of deep convection between north and south of the equator. Hereafter we refer to it as the eastern Pacific ITCZ dipole (EPID) mode, with the positive phase denoting a stronger northern than southern ITCZ. Note that the traditional index of Niño-3-mean precipitation averages out the EPID mode.

a. Coupled ocean–atmosphere feedback

Convective variability over the eastern tropical Pacific is coupled with SST. SST anomalies associated with the EPID are strong and positive north, while they are weak and negative south of the equator (Fig. 2c). From an atmospheric point of view, the cross-equatorial SST gradient intensifies the ITCZ north while weakening it south of the equator. The d4PDF atmospheric simulation, of sufficient resolution to resolve the double ITCZ, reproduces successfully the leading EOFs for FMA rainfall variability when forced with observed SST evolution (Fig. 5). The simulated PCs are highly correlated with observations.

South of the equator, the anomalous southeasterlies accelerate the southeast trade winds through the Coriolis effect (Figs. 2c and 5c), lowering SST with enhanced surface evaporation. North of the equator, in contrast, the easterly trade winds decelerate, helping increase SST with reduced evaporative cooling. This wind–evaporation–SST (WES) feedback preferentially amplifies the meridional coupled dipole pattern of SST and deep convection (Xie and Philander 1994). WES feedback and the resultant EPID are locked to the FMA season because the mean state is nearly symmetric and deep convection is sensitive to small changes in SST on either side of the equator. Theoretical studies indicate that the mean state with a symmetric off-equatorial double ITCZ is favorable for antisymmetric variability across the equator, compared to a northward-displaced ITCZ (Okajima et al.

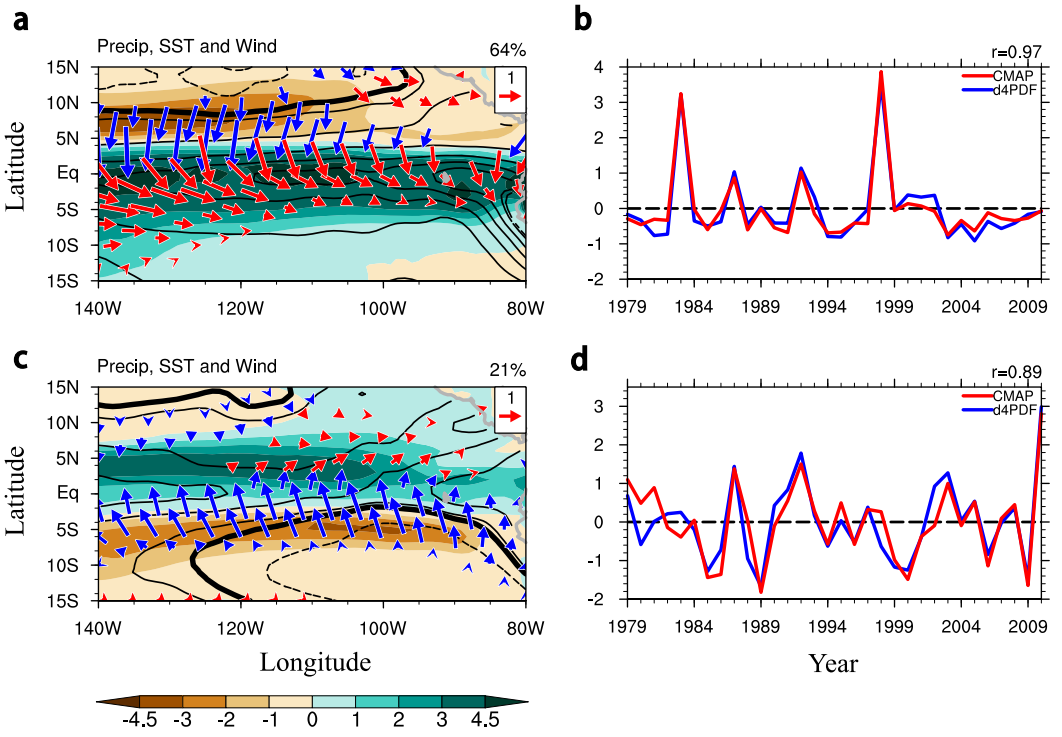

FIG. 5. EOFs of FMA rainfall variability in d4PDF atmospheric simulation. (a) EOF1 (shaded) for FMA rainfall variability over the eastern tropical Pacific, along with FMA surface wind (m s^{-1}, vectors,) and SST (contours at intervals of 0.3°C, zero thickened and negative dashed) regressed against the rainfall PC1. (b) Standardized PC1 for d4PDF (blue), and CMAP (red). (c),(d) As in (a),(b), but for EOF2. Blue (red) arrows indicate wind anomalies that strengthen (weaken) climatological winds. The correlations (r) are significant at the 95% confidence level based on a t test.

2003; Martinez-Villalobos and Vimont 2016). WES feedback mediates cross-equatorial interactions in the Atlantic basin. The Atlantic meridional mode is also most pronounced in FMA when the mean climate is nearly symmetric with the ITCZ sitting close to the equator (Chang et al. 2006; Deser et al. 2010).

b. *Evolution of moderate ENSO*

The observed PC2 is well correlated with concurrent central Pacific SST (r = 0.64 with Niño-4 SST) and a central Pacific El Niño index (Kao and Yu 2009) (r = 0.74). Since PC2 and Niño-4 SST are nearly symmetric between positive and negative events, we group these events and call them moderate ENSO as opposed to extreme El Niño (PC1). The terminology merely indicates the association of EPID with those ENSO events for which Niño-3 SST anomalies are moderate and eastern equatorial SSTs remain below the convective threshold. Two indices are generally necessary to classify specific ENSO events into two types (Takahashi et al. 2011; Cai et al. 2014).

ENSO is to first-order symmetric about the equator. Then how does a moderate ENSO transform into the antisymmetric EPID mode? At the peak phase of ENSO in the NDJ season, SST anomalies are indeed nearly symmetric about the equator (color shading in Fig. 6b). The mean SST, however, is strongly asymmetric over the eastern Pacific, above the convective threshold only north of the equator (color shading in Fig. 6a). As a result, the atmospheric response to symmetric SST anomalies is asymmetric about the equator. East of 140°W, deep convection intensifies only north of the equator during a moderate El Niño, accelerating the southeast trades on and south of the equator. This is consistent with vertical motion anomalies, with a deep structure over the entire troposphere north of the equator but trapped in the marine atmospheric boundary layer over the climatologically cool ocean surface on and south of the equator (Fig. 4a). The anomalous downward motion in the lower troposphere south of the equator is associated with increased stratiform cloud cover at the top of the marine boundary layer (Clement et al. 2009), reducing solar radiation that reaches the ocean surface (Fig. 7b). The reduced solar heating and enhanced surface evaporative cooling under the intensified southeast trades both act to lower SSTs south of the equator over the eastern Pacific.

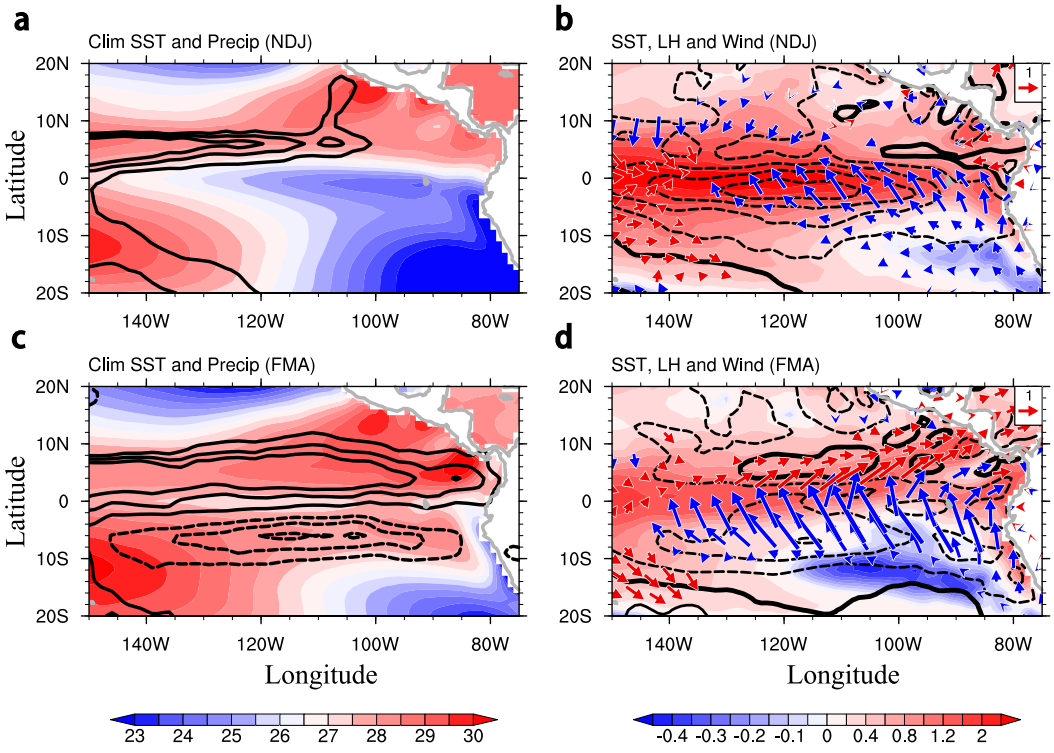

FIG. 6. Ocean–atmospheric anomalies of EPID. Regressions against the FMA rainfall PC2 for (a),(b) NDJ and (c),(d) FMA: (a),(c) rainfall (mm day^{-1}; contours at intervals of 1 mm day^{-1}, zero omitted and negative dashed); (b),(d) SST (°C; color shading), latent heat flux (W m^{-2}; contours with an interval of 5 W m^{-2}, zero contour thickened and negative dashed), and surface wind velocity (m s^{-1}; vectors), with blue (red) arrows indicating wind anomalies that strengthen (weaken) climatological winds. Also plotted in (a),(c) is climatological SST (°C; color shading).

This tendency of ocean surface cooling south of the equator triggers the WES feedback to grow the cross-equatorial dipole in the subsequent FMA season as SST anomalies are coupled with deep convection over the eastern Pacific across the equator. The prevailing cloud type changes from low/stratus to deep convective with season, resulting in a change in cloud-radiative effect on SST from negative in NDJ to positive in FMA as EPID develops with suppressed deep convection south of the equator at the shown polarity (Fig. 7b).

The beta effect is essential for WES feedback by accelerating the easterly trades in one hemisphere and decelerating them in the other. Xie (1996) shows that WES feedback is proportional to βY_I, where β is the northward gradient of the Coriolis parameter, and Y_I is the latitude of the off-equatorial double ITCZ symmetric about the equator. SST anomalies of moderate ENSO are not large enough to cause convection on the equator, triggering WES feedback instead that produces the EPID. Deep convection is possible only off the equator, with a finite $Y_I \sim 5°$. Extreme El Niño, on the other hand, activates deep convection on the equator, triggering the Bjerknes feedback with the westerly wind anomalies intruding into the eastern equatorial Pacific. WES feedback is not selected in this case, with no obvious choice for Y_I.

c. *Termination of moderate ENSO*

The EPID following a moderate El Niño is associated with pronounced southeasterly cross-equatorial wind anomalies (Figs. 2c and 7c), which drive a northward surface current on the equator where the Coriolis effect vanishes (Philander and Pacanowski 1981). A shallow overturning cell develops across the equator, with intensified ocean upwelling and decreased SST south the equator (Fig. 8b). Compared to December, El Niño warming in March shows moderate changes north of the equator but decays rapidly on and south of the equator as a result of the intensified south equatorial upwelling. This resembles the seasonal cooling of the eastern equatorial Pacific from April to September in response to the intensified southeast trades (Mitchell and Wallace 1992; Chang and Philander 1994). Thus, the rapid decay of moderate ENSO appears to be caused by cross-equatorial processes within 5°S–5°N that Niño-3 regional averages fail to represent.

Figure 8 presents the results from a simple heat budget analysis for the cross-equatorial (0°–10°N minus

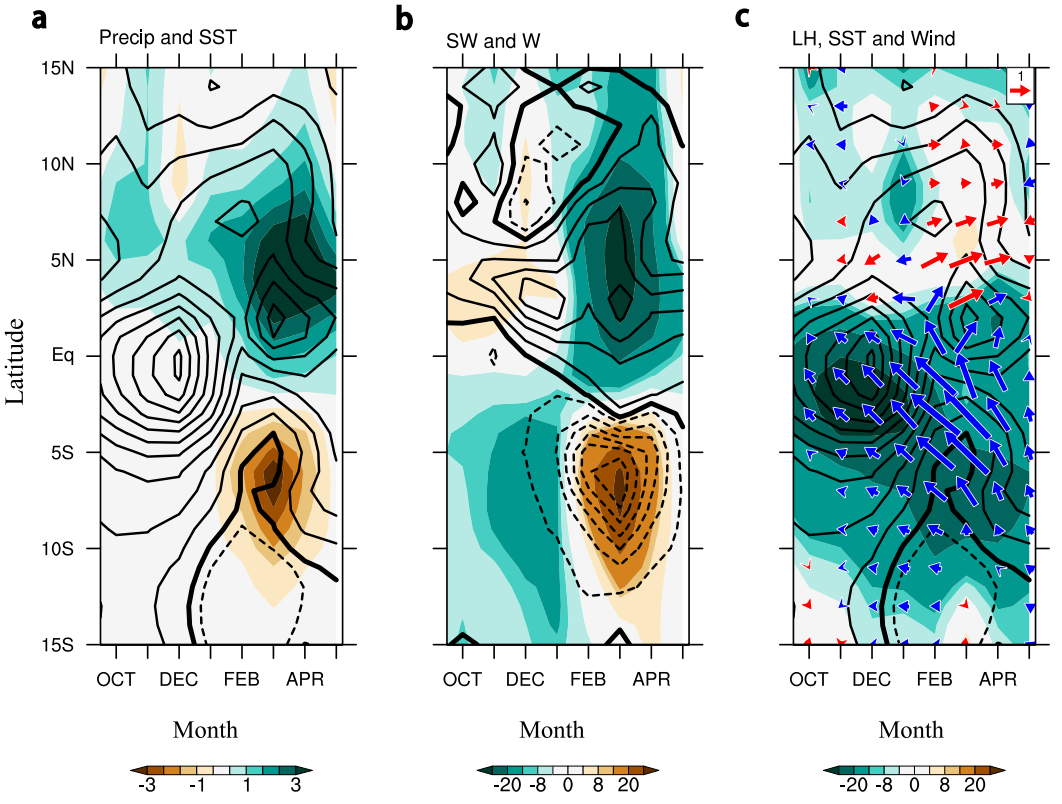

FIG. 7. Evolution of EPID. Regressions against the FMA rainfall PC2 as a function of calendar month and latitude: (a) SST (°C; contour) and precipitation (mm day^{-1}; shading); (b) downward solar radiation (SW) at the surface (shading in W m^{-2}) and vertical velocity (W) at 850 hPa (contours with an interval of 1 m s^{-1}, zero contour thickened and negative dashed); (c) SST (contours with an interval of 0.2°C, zero contour thickened and negative dashed), latent heat flux (LH, W m^{-2}; shading), and wind velocity (m s^{-1}; vectors), with increased (decreased) speed in blue (red). All zonally averaged in 140°–80°W.

0°–10°S) difference in perturbation SST (see the appendix for methods). The atmospheric effect on surface latent heat flux (notably WES) contributes to the development of the meridional asymmetry throughout the period from November to April. Shortwave cloud-radiative effects are a positive contributor at the peak phase of ENSO (NDJ; with stratus cloud feedback south of the equator) but subsequently turn into a strong damping when the south equatorial Pacific warms up and becomes conducive to deep convection. The ocean dynamical effect (e.g., the south-equatorial upwelling) becomes an important positive contributor to the meridional asymmetry during FMA in response to the pronounced cross-equatorial wind anomalies as the EPID develops. Work is under way to quantify the specific mechanisms for the EPID by using an ocean general circulation model. The results will be reported elsewhere.

The Pacific meridional mode (PMM) refers to coupled SST–surface wind anomalies that are forced in winter by atmospheric variability over the extratropical North Pacific and subsequently propagate southwestward toward the equator (Chiang and Vimont 2004; Ma et al. 2017b). The PMM often triggers moderate ENSO events upon arriving at the equator while the EPID mode develops in boreal spring and tends to follow moderate ENSO. Geographically, the PMM takes place over the North Pacific while EPID occurs over the eastern equatorial Pacific.

5. Variability over an extended period

Reliable satellite estimates of precipitation over oceans start from 1979. Here we extend our EOF analysis on FMA deep convective variability back to 1950 using ICOADS. Over convective regions, ship-observed marine cloudiness often reflects convective activity (Tokinaga et al. 2012). Back in time, ship meteorological reports were sparse over the eastern tropical Pacific except along a few shipping lanes. For robust results, we perform a joint EOF analysis on marine cloudiness, SST, and zonal and meridional components of the surface wind, all zonally averaged in 140°–80°W. The analysis is

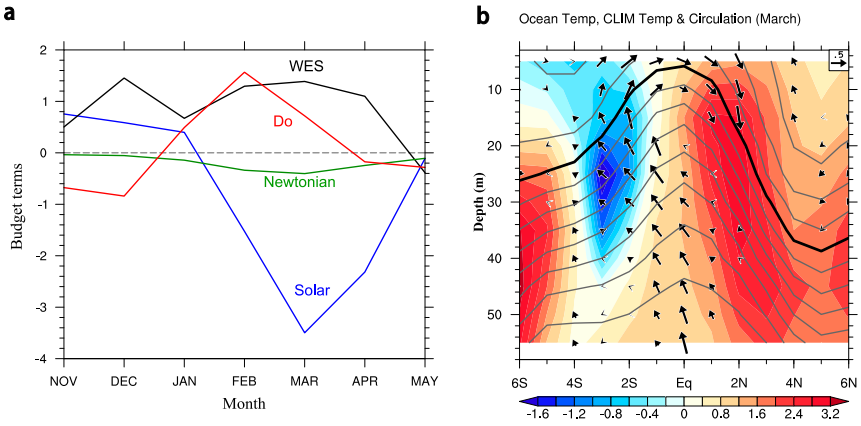

FIG. 8. Heat budget of EPID based on GODAS. (a) Cross-equatorial difference between 0°–10°N and 0°–10°S (zonally averaged in 140°–90°W) in terms of the ocean mixed layer budget (10^{-7} °C s^{-1}): surface solar radiation (blue line), surface latent heat flux [the sum of the Newtonian damping (green line) and atmospheric (notably WES) effect (black line)], and the residual due to ocean dynamical effects (D_O, red line). (b) Cross-equatorial transect of anomalous vertical circulation (arrows, m s^{-1} in meridional direction and 10^{-5} m s^{-1} in vertical direction) and ocean temperature (°C, color shading) in March at 90°W, along with the mean ocean temperature (line contours at 1°C intervals, with the 25°C contour highlighted).

done for FMA seasonal mean over a 68-yr period of 1950–2017.

The ICOADS joint EOF1, explaining 23% of the total combined variance, largely reproduces the precipitation EOF1 based on CMAP, with enhanced convection, positive SST, and westerly wind anomalies (Fig. 9b). The PC1 is strongly positively skewed.

The ICOADS joint EOF2, explaining 17% of the total combined variance, reproduces the CMAP precipitation EOF2. It features a meridional dipole of marine clouds,

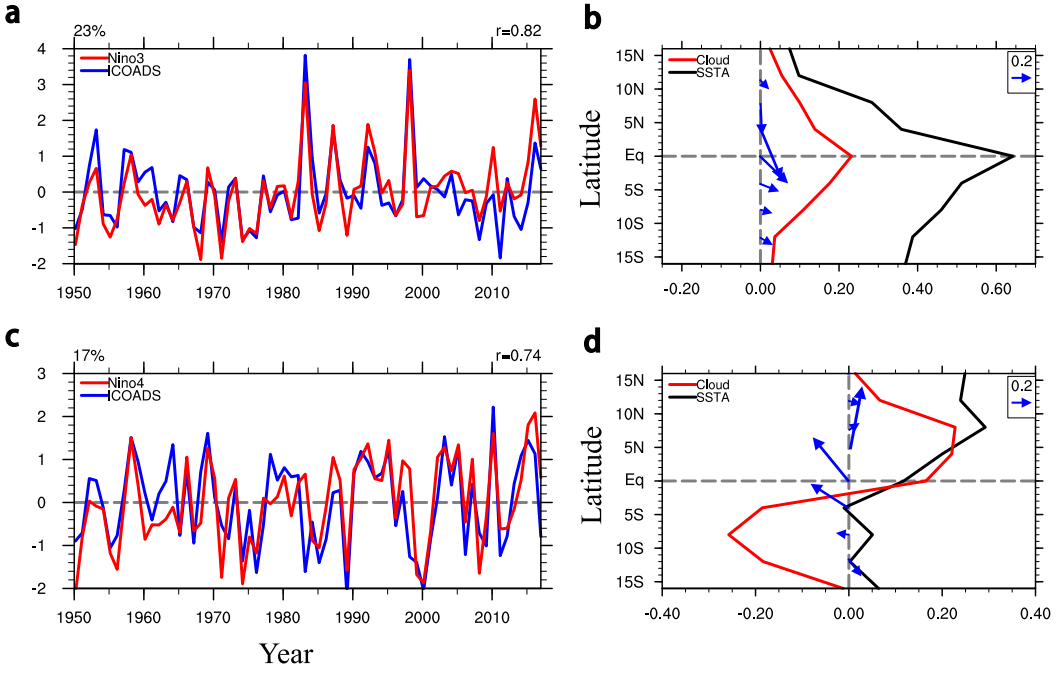

FIG. 9. Results from ICOADS ship observations. (a),(c) The standardized PCs (blue). Also plotted are (a) eastern (Niño-3) and (c) central (Niño-4) equatorial Pacific SST indices (standardized). (b),(d) Regressions of SSTA (°C; black), cloudiness (okta; red), and surface wind (m s^{-1}; vectors) against the ICOADS standardized PCs. The correlations between ICOADS and CMAP PCs are 0.87 (PC1) and 0.80 (PC2), respectively. The correlations (r) are significant at the 95% confidence level based on a t test.

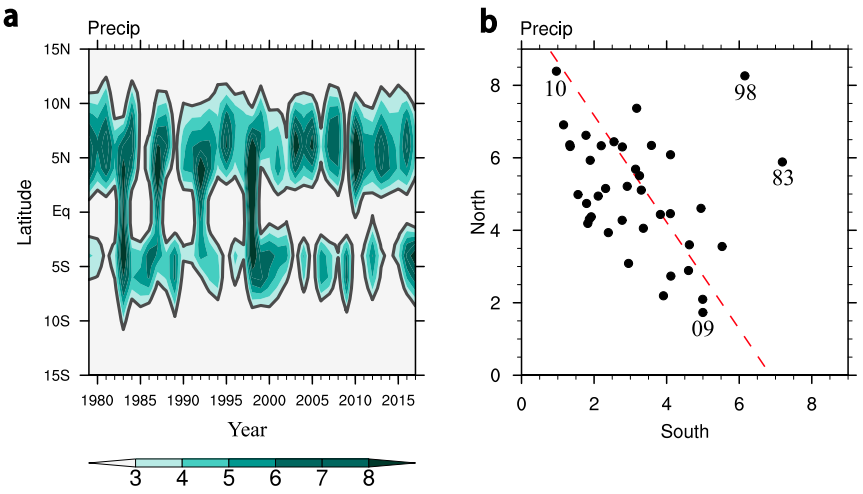

FIG. 10. MA mean precipitation. (a) Time–latitude section of MA precipitation (color shading in mm day^{-1}; the 2 mm day^{-1} contour highlighted in gray line) zonally averaged in 120°–100°W. (b) Scatter diagram for MA precipitation north (3°–10°N) and south (3°–10°S) of the equator.

coupled with meridional SST gradient and cross-equatorial wind anomalies that form WES feedback (Fig. 9d). Over the overlapping 39-yr period, the PC2s are highly correlated between ICOADS and CMAP (r = 0.80). The ICOADS PC2 is highly correlated with central Pacific (Niño-4) SST over the 68-yr period (r = 0.74). Thus, the EPID is a robust mode throughout the extended period after 1950 and is consistently triggered by moderate ENSO events. Specifically, the PC2 is one standard deviation below normal in FMA 1967 when the double ITCZ was first discovered from satellite images (Kornfield et al. 1967). The southern ITCZ is well developed in a negative EPID event while climatologically the ITCZ is stronger north than south of the equator (Fig. 1b).

We have performed the joint EOF on the zonal-mean precipitation, SST, and wind velocity based on ERA-20C and confirm that the PCs are highly correlated with those from ICOADS and with CMAP precipitation PCs. A recent independent study of Yu and Zhang (2018) showed that an anomalous strengthening of the southern ITCZ relative to the northern counterpart during FMA tends to be associated with a CP La Niña as previously noted from analysis of daily satellite images (Yang and Magnusdottir 2016). This is consistent with the correlation between the EPID mode and Niño-4 SST.

6. Summary and discussion

We have shown that interannual variability of eastern Pacific convection during FMA is organized into two coherent modes: one with intensified deep convection centered on the equator, and one with a meridional dipole with little signals on the equator. One can infer these modes from a scatter diagram for rainfall between the northern and southern ITCZ over the eastern Pacific (Fig. 10b); a negative correlation is apparent if the years 1983 and 1998 are excluded. These are years of extreme El Niño when deep convection intensifies on the climatologically cold equator (Fig. 10a). In FMA, the climatology features the nearly symmetric double ITCZ. Because of the EPID, there are years when only a single ITCZ appears, displaced either north (i.e., 2010) or south (i.e., 2009) of the equator. Here an ITCZ is recognized if the mean precipitation in 3°–10°N/S, 120°–100°W exceeds 2 mm day^{-1}. The scatter diagram in Fig. 10b indicates that EPID is nearly symmetric between the positive and negative phases, consistent with the EOF analysis for eastern Pacific precipitation (Fig. 2d).

In FMA, the eastern equatorial Pacific mean state allows either Bjerknes or WES feedback to occur. It is the time when equatorial SSTs reach the annual maximum and a strong enough El Niño can cause deep convection on the equator and drive the westerly wind anomalies to intrude into the eastern Pacific (Fig. 11a). The reduced equatorial trades suppress the equatorial upwelling, allowing the El Niño warming to linger despite a thermocline that has shoaled back. We note that the eastward intrusion of the westerly anomalies during extreme El Niño is more in line with what Bjerknes (1969) originally envisioned than the classic view of El Niño (Wyrtki 1975; Deser and Wallace 1990) that is applicable to moderate ENSO.

For moderate El Niño, equatorial SSTs are not high enough to trigger deep convection, and WES feedback is selected in FMA instead. Weak asymmetries in NDJ SST anomalies as a result of the meridional asymmetry in the mean state grow into an antisymmetric EPID mode

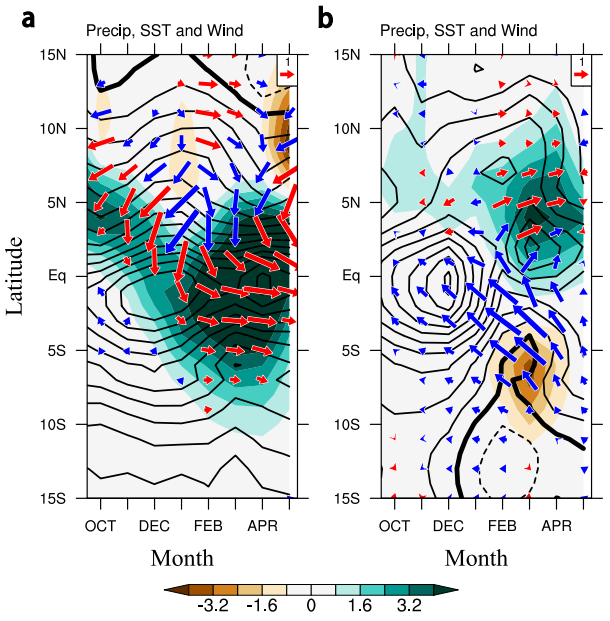

FIG. 11. Evolution of (a) extreme and (b) moderate El Niño. Anomalies of precipitation (mm day^{-1}; color shading), SST (°C; contours at 0.2°C intervals; zero contour thickened), and surface wind (m s^{-1}; vectors) regressed against the FMA rainfall PC1 and PC2 as a function of calendar month and latitude. All zonally averaged in 140°–80°W. Blue (red) arrows indicate wind anomalies that strengthen (weaken) climatological winds.

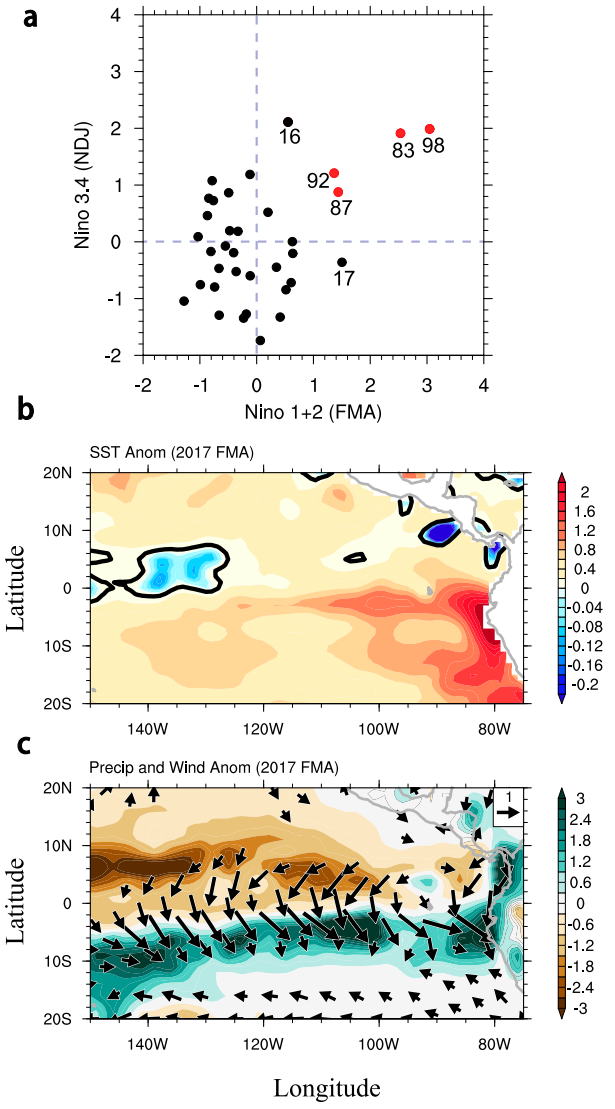

FIG. 12. (a) Scatter diagram between NDJ Niño-3.4 and FMA Niño-1+2 SST indices (°C) for 1982–2017, the former widely used to track ENSO. Anomalies in FMA 2017: (b) SST (°C, shaded; the zero contour in black), and (c) rainfall (mm day^{-1}; shaded) and surface wind (m s^{-1}; vectors).

(Fig. 11b). The anomalous southeasterlies intensify ocean upwelling south of the equator, causing the El Niño warming to decay rapidly on and south of the equator.

The ongoing debate on ENSO diversity focuses on the SST pattern at the peak phase (Kao and Yu 2009; Ashok et al. 2007; Capotondi et al. 2015; Kug et al. 2009). From the perspective of eastern Pacific convection, our study supports the view that canonical ENSO oscillates between moderate El Niño and La Niña while extreme El Niño is in a rare class of its own (Cai et al. 2014; Takahashi and Dewitte 2016). We show that the two ENSO types follow distinct decay trajectories in FMA shaped by different coupled feedbacks over the eastern tropical Pacific. Extreme El Niño decays slowly and sustains a strong equatorial warming through positive feedback with enhanced convection and westerly wind anomalies in the eastern Pacific, while moderate ENSO dissipates quickly in the eastern Pacific as WES feedback selectively amplifies the antisymmetric EPID in FMA and the enhanced southeast trades intensify ocean upwelling south of the equator. Perhaps as a consequence, moderate ENSO tends to be of the central Pacific type (Kao and Yu 2009) in the SST anomaly pattern.

The 2015/16 El Niño is a major event by the metric of NDJ Niño-3.4 SST. Niño-3 SST was high in NDJ at 2.8°C but dropped by a whopping 1.9°C from January to only 0.9°C in April 2016. Both PC1 and PC2 are only moderately positive in FMA 2016, suggesting that there are independent mechanisms for the zonal pattern of El Niño warming other than the magnitude of Niño-3 SST and EPID.

El Niño derives its name from anomalous coastal warming off Peru but now commonly refers to the basin-scale warming events. On the normally dry Pacific coast of Peru, coastal warming events are important for heavy rainfall and floods in FMA when climatological SSTs are at the annual maximum and approach the convective threshold. Extreme El Niño is followed by major coastal warming off Peru (Fig. 12a),

presumably through the deepened thermocline across the eastern Pacific. FMA Peruvian coastal warming is not generally preceded by a basin-scale Niño, however. Excluding four extreme El Niños of 1983, 1987, 1992, and 1998, in fact, FMA Niño-1+2 and NDJ Niño-3.4 SST indices are not significantly correlated. The strong coastal warming event of 2017 was even preceded by a weak basin-scale La Niña. In March 2017, torrential rains devastated northern Peru, flooding towns and cities and causing severe socioeconomic hardships. At Piura, Peru, accumulated rainfall reached 631 mm during three months of January–March 2017, as compared to the annual climatology of 75 mm. Extreme high SSTs in excess of 28.5°C were observed off Peru, promoting atmospheric deep convection in the coastal region. In March 2017, a zonal band of increased rainfall extends from coastal Peru across half of the Pacific basin south of the equator, paired with a band of decreased rainfall just north of the equator (Fig. 12c), reminiscent of the EPID. Takahashi and Martínez (2017) noted a similar coastal El Niño event in 1925 that was preceded by a basin-scale La Niña, and discussed the effects of local and Niño-4 SST. In general, however, Niño-1+2 SST is not significantly correlated with our FMA rainfall PC2. More research is needed to study coupled processes for ENSO diversity, between moderate ENSO and extreme El Niño as well as between basin-scale and coastal El Niño.

Acknowledgments. Q. P. and S.-P. X. contributed equally. This work is supported by the U.S. National Science Foundation (1637450), the National Key R&D Program of China (2016YFA0601804), the Strategic Priority Research Programs of the Chinese Academy of Sciences (XDA11010302), the National Natural Science Foundation of China (41521005), and China Scholarship Council (201604910798).

APPENDIX

A Mixed Layer Heat Budget

Here we use a simple mixed layer heat budget to estimate contributions of different physical processes to SST changes,

$$\frac{\partial \mathrm{T}}{\partial \mathrm{t}} = \frac{Q_S + Q_E + Q_L + Q_H}{\rho c_P H} + D_o, \qquad \text{(A1)}$$

where T is the perturbation temperature averaged over the mixed layer; ρ and c_p are density and specific heat capacity of seawater, respectively; and H is the mean mixed layer depth defined as the depth at which the temperature is 0.5°C lower than the SST. Here Q_S is the shortwave perturbations absorbed by the mixed layer. We decompose the surface latent heat flux (LHF) perturbation Q_E into components resulting from SST and atmospheric changes, respectively,

$$Q_E = Q_N + Q_A, \qquad \text{(A2)}$$

where $Q_N = \overline{Q}_E \alpha T$ is the Newtonian damping on SST change caused by evaporation (Du et al. 2009). Here the overbar denotes the climatological mean and the prime denoting the perturbation is omitted for brevity, $\alpha = 1/q_s \; dq_s/dT$, and q_s is the saturated specific humidity following the Clausius–Clapeyron equation. The term Q_A in Eq. (A2) is the LHF perturbation induced by atmospheric (notably wind) changes, obtained as the residual, $Q_A = Q_E - Q_N$. If relative humidity is a constant and the surface air–sea temperature difference is neglected, $Q_A = \overline{Q}_E W/\overline{W}$ represents the WES effect, where W is the scalar wind speed. Longwave radiation (Q_L) and sensible heat flux (Q_H) perturbations are very small and omitted here.

The last term (D_O) on the rhs of Eq. (A1) represents the effect of ocean dynamical processes such as advection and mixing. Here we estimate the total ocean dynamical effect as the residual of Eq. (A1). Quantifying contributions of specific oceanic processes such as horizontal advection and upwelling and closing the budget require carefully designed output of relevant terms, a task we plan to pursue as a future study. Figure 8 shows the cross-equatorial difference in major terms in Eq. (A1) between the north (0°–10°N) and south (0°–10°S) equatorial Pacific, zonally averaged in 140°–90°W.

REFERENCES

Ashok, K., S. K. Behera, S. A. Rao, H. Weng, and T. Yamagata, 2007: El Niño Modoki and its possible teleconnection. *J. Geophys. Res.*, **112**, C11007, https://doi.org/10.1029/2006JC003798.

Bjerknes, J., 1969: Atmospheric teleconnections from the equatorial Pacific. *Mon. Wea. Rev.*, **97**, 163–172, https://doi.org/10.1175/1520-0493(1969)097<0163:ATFTEP>2.3.CO;2.

Cai, W. J., and Coauthors, 2014: Increasing frequency of extreme El Niño events due to greenhouse warming. *Nat. Climate Change*, **4**, 111–116, https://doi.org/10.1038/nclimate2100.

Capotondi, A., and Coauthors, 2015: Understanding ENSO diversity. *Bull. Amer. Meteor. Soc.*, **96**, 921–938, https://doi.org/10.1175/BAMS-D-13-00117.1.

Chang, P., and Coauthors, 2006: Climate fluctuations of tropical coupled systems—The role of ocean dynamics. *J. Climate*, **19**, 5122–5174, https://doi.org/10.1175/JCLI3903.1.

——, and S. G. Philander, 1994: A coupled ocean–atmosphere instability of relevance to the seasonal cycle. *J. Atmos. Sci.*, **51**, 3627–3648, https://doi.org/10.1175/1520-0469(1994)051<3627:ACOIOR>2.0.CO;2.

Chiang, J. C. H., and D. J. Vimont, 2004: Analagous meridional modes of atmosphere–ocean variability in the tropical Pacific

and tropical Atlantic. *J. Climate*, **17**, 4143–4158, https://doi.org/10.1175/JCLI4953.1.

Chiodi, A. M., and D. E. Harrison, 2013: El Niño impacts on seasonal U.S. atmospheric circulation, temperature, and precipitation anomalies: The OLR-event perspective. *J. Climate*, **26**, 822–837, https://doi.org/10.1175/JCLI-D-12-00097.1.

Clement, A. C., R. Burgman, and J. R. Norris, 2009: Observational and model evidence for positive low-level cloud feedback. *Science*, **325**, 460–464, https://doi.org/10.1126/science.1171255.

Dee, D. P., and Coauthors, 2011: The ERA-Interim reanalysis: Configuration and performance of the data assimilation system. *Quart. J. Roy. Meteor. Soc.*, **137**, 553–597, https://doi.org/10.1002/qj.828.

Deser, C., and J. M. Wallace, 1990: Large-scale atmospheric circulation features of warm and cold episodes in the tropical Pacific. *J. Climate*, **3**, 1254–1281, https://doi.org/10.1175/1520-0442(1990)003<1254:LSACFO>2.0.CO;2.

——, M. A. Alexander, S.-P. Xie, and A. S. Phillips, 2010: Sea surface temperature variability: Patterns and mechanisms. *Annu. Rev. Mar. Sci.*, **2**, 115–143, https://doi.org/10.1146/annurev-marine-120408-151453.

Du, Y., S.-P. Xie, G. Huang, and K. Hu, 2009: Role of air–sea interaction in the long persistence of El Niño–induced north Indian Ocean warming. *J. Climate*, **22**, 2023–2038, https://doi.org/10.1175/2008JCLI2590.1.

Freeman, E., and Coauthors, 2017: ICOADS release 3.0: A major update to the historical marine climate record. *Int. J. Climatol.*, **37**, 2211–2232, https://doi.org/10.1002/joc.4775.

Huang, B., and Coauthors, 2015: Extended reconstructed sea surface temperature version 4 (ERSST.v4): Part I: Upgrades and intercomparisons. *J. Climate*, **28**, 911–930, https://doi.org/10.1175/JCLI-D-14-00006.1.

Johnson, N. C., and S.-P. Xie, 2010: Changes in the sea surface temperature threshold for tropical convection. *Nat. Geosci.*, **3**, 842–845, https://doi.org/10.1038/ngeo1008.

——, and Y. Kosaka, 2016: The impact of eastern equatorial Pacific convection on the diversity of boreal winter El Niño teleconnection patterns. *Climate Dyn.*, **47**, 3737–3765, https://doi.org/10.1007/s00382-016-3039-1.

Kao, H. Y., and J. Y. Yu, 2009: Contrasting eastern-Pacific and central-Pacific types of ENSO. *J. Climate*, **22**, 615–632, https://doi.org/10.1175/2008JCLI2309.1.

Kornfield, J., A. F. Hasler, K. J. Hanson, and V. E. Suomi, 1967: Photographic cloud climatology from ESSA III and V computer produced mosaics. *Bull. Amer. Meteor. Soc.*, **48**, 878–883.

Kug, J. S., F. F. Jin, and S. I. An, 2009: Two types of El Niño events: Cold tongue El Niño and warm pool El Niño. *J. Climate*, **22**, 1499–1515, https://doi.org/10.1175/2008JCLI2624.1.

Kumar, B. P., J. Vialard, M. Lengaigne, V. S. N. Murty, and M. J. McPhaden, 2012: TropFlux: Air-sea fluxes for the global tropical oceans—Description and evaluation. *Climate Dyn.*, **38**, 1521–1543, https://doi.org/10.1007/s00382-011-1115-0.

Lee, T., and M. J. McPhaden, 2010: Increasing intensity of El Niño in the central-equatorial Pacific. *Geophys. Res. Lett.*, **37**, L14603, https://doi.org/10.1029/2010GL044007.

Lengaigne, M., and G. A. Vecchi, 2010: Contrasting the termination of moderate and extreme El Niño events in coupled general circulation models. *Climate Dyn.*, **35**, 299–313, https://doi.org/10.1007/s00382-009-0562-3.

Ma, J., S.-P. Xie, and H. Xu, 2017a: Intermember variability of the summer northwest Pacific subtropical anticyclone in the ensemble forecast. *J. Climate*, **30**, 3927–3941, https://doi.org/10.1175/JCLI-D-16-0638.1.

——, ——, and ——, 2017b: Contributions of the North Pacific Meridional Mode to ensemble spread of ENSO prediction. *J. Climate*, **30**, 9167–9181, https://doi.org/10.1175/JCLI-D-17-0182.1.

Martinez-Villalobos, C., and D. J. Vimont, 2016: The role of the mean state in meridional mode structure and growth. *J. Climate*, **29**, 3907–3921, https://doi.org/10.1175/JCLI-D-15-0542.1.

McGregor, S., A. Timmermann, N. Schneider, M. F. Stuecker, and M. H. England, 2012: The effect of the South Pacific convergence zone on the termination of El Niño events and the meridional asymmetry of ENSO. *J. Climate*, **25**, 5566–5586, https://doi.org/10.1175/JCLI-D-11-00332.1.

McPhaden, M. J., 1999: Genesis and evolution of the 1997-98 El Niño. *Science*, **283**, 950–954, https://doi.org/10.1126/science.283.5404.950.

Mitchell, T. P., and J. M. Wallace, 1992: The annual cycle in equatorial convection and sea surface temperature. *J. Climate*, **5**, 1140–1156, https://doi.org/10.1175/1520-0442(1992)005<1140:TACIEC>2.0.CO;2.

Mizuta, R., and Coauthors, 2017: Over 5,000 years of ensemble future climate simulations by 60-km global and 20-km regional atmospheric models. *Bull. Amer. Meteor. Soc.*, **98**, 1383–1398, https://doi.org/10.1175/BAMS-D-16-0099.1.

Ohba, M., and H. Ueda, 2006: A role of zonal gradient of SST between the Indian Ocean and the western Pacific in localized convection around the Philippines. *SOLA*, **2**, 176–179, https://doi.org/10.2151/sola.2006-045.

Okajima, H., S.-P. Xie, and A. Numaguti, 2003: Interhemispheric coherence of tropical climate variability: Effect of the climatological ITCZ. *J. Meteor. Soc. Japan*, **81**, 1371–1386, https://doi.org/10.2151/jmsj.81.1371.

Okumura, Y. M., and C. Deser, 2010: Asymmetry in the duration of El Niño and La Niña. *J. Climate*, **23**, 5826–5843, https://doi.org/10.1175/2010JCLI3592.1.

Philander, S. G. H., and R. C. Pacanowski, 1981: The oceanic response to cross-equatorial winds (with application to coastal upwelling in low latitudes). *Tellus*, **33**, 201–210, https://doi.org/10.3402/tellusa.v33i2.10708.

Poli, P., and Coauthors, 2016: ERA-20C: An atmospheric reanalysis of the twentieth century. *J. Climate*, **29**, 4083–4097, https://doi.org/10.1175/JCLI-D-15-0556.1.

Reynolds, R. W., N. A. Rayner, T. M. Smith, D. C. Stokes, and W. Q. Wang, 2002: An improved in situ and satellite SST analysis for climate. *J. Climate*, **15**, 1609–1625, https://doi.org/10.1175/1520-0442(2002)015<1609:AIISAS>2.0.CO;2.

Siler, N., Y. Kosaka, S.-P. Xie, and X. Li, 2017: Tropical ocean contributions to California's surprisingly dry El Niño of 2015/16. *J. Climate*, **30**, 10 067–10 079, https://doi.org/10.1175/JCLI-D-17-0177.1.

Takahashi, K., and B. Dewitte, 2016: Strong and moderate nonlinear El Niño regimes. *Climate Dyn.*, **46**, 1627–1645, https://doi.org/10.1007/s00382-015-2665-3.

——, and A. G. Martínez, 2017: The very strong coastal El Niño in 1925 in the far-eastern Pacific. *Climate Dyn.*, https://doi.org/10.1007/s00382-017-3702-1, in press.

——, A. Montecinos, K. Goubanova, and B. Dewitte, 2011: ENSO regimes: Reinterpreting the canonical and Modoki El Niño. *Geophys. Res. Lett.*, **38**, L10704, https://doi.org/10.1029/2011GL047364.

Takayabu, Y. N., T. Iguchi, M. Kachi, A. Shibata, and H. Kanzawa, 1999: Abrupt termination of the 1997-98 El Niño in response

to a Madden–Julian oscillation. *Nature*, **402**, 279–282, https://doi.org/10.1038/46254.

Tokinaga, H., S.-P. Xie, A. Timmermann, S. McGregor, T. Ogata, H. Kubota, and Y. M. Okumura, 2012: Regional patterns of tropical Indo-Pacific climate change: Evidence of the Walker circulation weakening. *J. Climate*, **25**, 1689–1710, https://doi.org/10.1175/JCLI-D-11-00263.1.

Vecchi, G. A. and D. E. Harrison, 2006: The termination of the 1997–98 El Niño. Part I: Mechanisms of oceanic change. *J. Climate*, **19**, 2633–2646, https://doi.org/10.1175/JCLI3776.1.

Wyrtki, K., 1975: El Niño—The dynamic response of the equatorial Pacific Ocean to atmospheric forcing. *J. Phys. Oceanogr.*, **5**, 572–584, https://doi.org/10.1175/1520-0485(1975)005<0572:ENTDRO>2.0.CO;2.

Xie, P., and P. A. Arkin, 1997: Global precipitation: A 17-year monthly analysis based on gauge observations, satellite estimates, and numerical model outputs. *Bull. Amer. Meteor. Soc.*, **78**, 2539–2558, https://doi.org/10.1175/1520-0477(1997)078<2539:GPAYMA>2.0.CO;2.

Xie, S.-P., 1994: On the genesis of the equatorial annual cycle. *J. Climate*, **7**, 2008–2013, https://doi.org/10.1175/1520-0442(1994)007<2008:OTGOTE>2.0.CO;2.

——, 1996: Westward propagation of latitudinal asymmetry in a coupled ocean–atmosphere model. *J. Atmos. Sci.*, **53**, 3236–3250, https://doi.org/10.1175/1520-0469(1996)053<3236:WPOLAI>2.0.CO;2.

——, 2004: The shape of continents, air-sea interaction and the rising branch of the Hadley circulation. *The Hadley Circulation: Past, Present and Future*, H. F. Diaz and R. S. Bradley, Eds., Kluwer Academic Publishers, 121–152.

——, and S. G. H. Philander, 1994: A coupled ocean-atmosphere model of relevance to the ITCZ in the eastern Pacific. *Tellus*, **46A**, 340–350, https://doi.org/10.3402/tellusa.v46i4.15484.

——, Y. Du, G. Huang, X.-T. Zheng, H. Tokinaga, K. Hu, and Q. Liu, 2010: Decadal shift in El Niño influences on Indo–western Pacific and East Asian climate in the 1970s. *J. Climate*, **23**, 3352–3368, https://doi.org/10.1175/2010JCLI3429.1.

Yang, L., X. Wang, K. Huang, and D. Wang, 2015: Anomalous tropical cyclone activity in the western North Pacific in August 2014. *Bull. Amer. Meteor. Soc.*, **96**, S120–S125, https://doi.org/10.1175/BAMS-D-15-00125.1.

Yang, W., and G. Magnusdottir, 2016: Interannual signature in daily ITCZ states in the east Pacific in boreal spring. *J. Climate*, **29**, 8013–8025, https://doi.org/10.1175/JCLI-D-16-0395.1.

Yu, H. Y., and M. H. Zhang, 2018: Explaining the year-to-year variability of the eastern Pacific intertropical convergence zone in the boreal spring. *J. Geophys. Res. Atmos.*, https://doi.org/10.1002/2017JD028156, in press.

Zheng, X. T., S.-P. Xie, L. H. Lv, and Z. Q. Zhou, 2016: Intermodel uncertainty in ENSO amplitude change tied to Pacific Ocean warming pattern. *J. Climate*, **29**, 7265–7279, https://doi.org/10.1175/JCLI-D-16-0039.1.